



HAL
open science

Understanding the STM images of epitaxial graphene on a reconstructed 6H-SiC(0001) surface: the role of tip-induced mechanical distortion of graphene

José A. Morán-Meza, Jacques Cousty, Christophe Lubin, François Thoyer

► To cite this version:

José A. Morán-Meza, Jacques Cousty, Christophe Lubin, François Thoyer. Understanding the STM images of epitaxial graphene on a reconstructed 6H-SiC(0001) surface: the role of tip-induced mechanical distortion of graphene. *Physical Chemistry Chemical Physics*, 2016, 18, pp.14264. 10.1039/C5CP07571H . cea-01485270

HAL Id: cea-01485270

<https://cea.hal.science/cea-01485270>

Submitted on 8 Mar 2017

HAL is a multi-disciplinary open access archive for the deposit and dissemination of scientific research documents, whether they are published or not. The documents may come from teaching and research institutions in France or abroad, or from public or private research centers.

L'archive ouverte pluridisciplinaire **HAL**, est destinée au dépôt et à la diffusion de documents scientifiques de niveau recherche, publiés ou non, émanant des établissements d'enseignement et de recherche français ou étrangers, des laboratoires publics ou privés.



Cite this: *Phys. Chem. Chem. Phys.*,
2016, **18**, 14264

Understanding the STM images of epitaxial graphene on a reconstructed 6H-SiC(0001) surface: the role of tip-induced mechanical distortion of graphene†

José A. Morán-Meza,^{*ab} Jacques Cousty,^{*a} Christophe Lubin^a and François Thoyer^a

Epitaxial graphene (EG) grown on an annealed 6H-SiC(0001) surface has been studied under ultra-high vacuum (UHV) conditions by using a combined dynamic-scanning tunneling microscope/frequency modulation-atomic force microscope (dynamic-STM/FM-AFM) platform based on a qPlus probe. STM and AFM images independently recorded present the same hexagonal lattice of bumps with a 1.9 nm lattice period, which agrees with density functional theory (DFT) calculations and experimental results previously reported, attributed to the (6×6) quasi-cell associated with the 6H-SiC(0001) $(6\sqrt{3} \times 6\sqrt{3})R30^\circ$ reconstruction. However, topographic bumps in AFM images and maxima in the simultaneously recorded mean-tunneling-current map do not overlap but appear to be spaced typically by about 1 nm along the [11] direction of the (6×6) quasi-cell. A similar shift is observed between the position of maxima in dynamic-STM images and those in the simultaneously recorded frequency shift map. The origin of these shifts is discussed in terms of electronic coupling variations between the local density of states (LDOS) of EG and the LDOS of the buffer layer amplified by mechanical distortions of EG induced by the STM or AFM tip. Therefore, a constant current STM image of EG on a reconstructed 6H-SiC(0001) surface does not reproduce its real topography but corresponds to the measured LDOS modulations, which depend on the variable tip-induced graphene distortion within the (6×6) quasi-cell.

Received 8th December 2015,
Accepted 4th March 2016

DOI: 10.1039/c5cp07571h

www.rsc.org/pccp

1. Introduction

Graphene, a single layer of sp^2 bonded carbon atoms arranged in a honeycomb lattice, is a material widely studied by the scientific community because of its electrical, magnetic, optical, thermal and mechanical properties and it appears to be a promising material for numerous technological applications.¹ Since the first production of graphene in 2004,² several production methods have been developed to synthesize graphene^{1,3,4} and it was found that the method of graphene synthesis drastically influences its properties.⁵ However, the thermal-decomposition method of commercial silicon carbide (SiC) crystals,^{4,6} which yields epitaxial graphene (EG) grown on a semiconductor 6H-SiC(0001) substrate, is considered a particularly promising method for the production of high-quality large-scale graphene for high speed electronic devices since no additional transfer procedure of graphene onto another substrate is required.^{7–9}

The structure of graphene on a 6H-SiC(0001) surface has been intensively investigated mainly by low energy electron diffraction^{4,6,10–15} and scanning tunneling microscopy (STM).^{10,11,14–24} Nevertheless, only a few experimental high-resolution atomic force microscopy (AFM) studies, by using a cantilever^{6,25–27} or a quartz crystal resonator with an integrated tip (qPlus sensor),²⁸ and theoretical studies, by using a numerical AFM in frequency modulation (FM) mode,²⁹ have been reported, revealing the topography of EG on the 6H-SiC(0001) surface. Recently, atomic resolution was achieved for quasi-freestanding monolayer graphene on 6H-SiC(0001) with a qPlus probe in air.³⁰

From these experimental studies, the following model emerges: during the thermal growth of graphene from a 6H-SiC(0001) surface, a carbon-rich interface layer characterized by the $(6\sqrt{3} \times 6\sqrt{3})R30^\circ$ structure (hereafter called the “buffer layer”¹⁵) is first formed on the substrate and then EG grows on this carbon overlayer. STM images of EG on the buffer layer exhibit two lattices: a hexagonal arrangement of bumps with a 1.9 nm lattice period, which is described by a (6×6) quasi-cell,^{11,17,18,31} and a honeycomb lattice resting on the periodic corrugations of the buffer layer that corresponds to graphene. By using an ultra-high vacuum (UHV) non-contact AFM, Filleter and Bennewitz^{25,26} obtained the AFM topography of graphene on 6H-SiC(0001) that shows a

^a SPEC, CEA, CNRS, Université Paris-Saclay, CEA Saclay 91191 Gif-sur-Yvette Cedex, France. E-mail: jacques.cousty@cea.fr

^b Grupo de Materiales Nanoestructurados, Facultad de Ciencias, Universidad Nacional de Ingeniería, Av. Túpac Amaru 210, Lima 25, Peru. E-mail: jmoranm@uni.edu.pe, jose.moran.meza@gmail.com

† Electronic supplementary information (ESI) available. See DOI: 10.1039/c5cp07571h

hexagonal lattice with a 1.9 nm lattice period identified with the (6 × 6) quasi-cell, though the operating conditions had not been reported.

Density functional theory (DFT) and *ab initio* studies of the EG on 6H-SiC(0001) were developed by Mattausch *et al.*,³² Varchon *et al.*^{19,33} and Kim *et al.*³⁴ The simulated STM images of a graphene layer above the buffer layer obtained by Kim *et al.*,³⁴ from calculations of the local density of states (LDOS) at the Fermi level, show a lattice with a 1.9 nm period related to the (6 × 6) quasi-cell defined by the LDOS maxima, as observed in experimental STM images.^{11,17,18,31} Additionally, this (6 × 6) quasi-cell is comprised of two triangular regions that present an asymmetric contrast.^{11,35–37} On the other hand, the atomic structure of the graphene layer above the buffer layer obtained by Varchon *et al.*,¹⁹ from calculations of total DOS, also presents a (6 × 6) quasi-cell defined by the total DOS maxima, as shown in Fig. 4(a) of ref. 19. Such a structure complies with the (6 × 6) quasi-cell identified in high-resolution AFM topographies.^{25,26} Remarkably, these DFT studies^{19,33,34} indicated that the total DOS maxima and LDOS maxima of EG were overlaid. These models also show that EG follows the surface corrugation of the buffer layer underneath it but presents a lower surface corrugation (34 pm³⁴ or 40 pm¹⁹) than that of the buffer layer (120 pm¹⁹). Accordingly, the separation distance between the graphene layer and the buffer layer is found to be modulated along the [11] direction of the (6 × 6) quasi-cell. Due to this modulated distance, we have shown that both STM and AFM tips provoke some distortion of the graphene layer during the scanning process.³⁸

Other examples of tip-induced distortions of graphene layers have been reported for graphene grown on several substrates. A strong tip–surface interaction provokes lateral displacements of ridges observed on EG on 6H-SiC(0001) by STM.³⁹ Also, STM studies of supported graphene on the SiO₂ substrate⁴⁰ as well as the suspended graphene membrane⁴¹ led to the conclusion that the graphene layer is deformed due to strong interactions between the STM tip and the graphene layer. On the other hand, a reversible deformation of a graphene monolayer has been evidenced for EG on Ru(0001) for an AFM tip operated in an attractive regime.⁴² Moreover, Giessibl *et al.*⁴³ and Kawai *et al.*⁴⁴ reported repulsive tip–sample interactions during measurements in constant-height of a highly oriented pyrolytic graphite (HOPG) surface (conformed by many graphene sheets), by using a combined UHV STM/AFM operating a low and room temperatures, respectively. However, the studies of graphene on metal surfaces (graphene on Rh(111)⁴⁵ and graphene on Ir(111)⁴⁶) revealed that the tunneling current occurs when the tip is interacting in the attractive regime. Recently, during STM studies of graphene on Ir(111), Altenburg *et al.*⁴⁷ showed that the graphene sheet gets significantly lifted *via* van der Waals forces between the graphene and STM tip. However, for the same system, Dedkov *et al.*⁴⁶ measured a force gradient of 2.21 N m^{−1} (repulsive regime) during constant-height AFM experiments. From the analysis of these STM or AFM studies of graphene growth on metal and 6H-SiC(0001) surfaces, the graphene suffers from general distortion induced by the STM or AFM tip. Keeping in mind the

giant corrugation observed in the STM image of graphite⁴⁸ and confirmed by AFM measurements,⁴⁴ the question arises about the consequences of tip-induced distortion of EG on the reconstructed 6H-SiC(0001) surface on the corresponding STM images.

Here, we present a study of the structural and electrical properties of EG on a 6H-SiC(0001) surface under UHV at room temperature (RT) using a combined dynamic STM/FM-AFM microscope, based on a qPlus sensor equipped with a conductive tip. The tip having a sub-nanometric oscillation amplitude allows for this microscope to record images using two techniques: (1) AFM topography with simultaneous maps of mean tunneling current $\langle I_T \rangle$ and excitation variations E_{exc} ; and (2) dynamic-STM image with simultaneous maps of force gradient $\left(k_{\text{ts}} = -\frac{\partial F_{\text{ts}}}{\partial z} \right)$ and excitation variations E_{exc} . Finally, the origin of some of the contrast differences observed between the dynamic-STM image with k_{ts} map (AFM topography with $\langle I_T \rangle$ map) will be discussed in terms of coupling changes between the local density of states (LDOS) of EG and the LDOS of the buffer layer amplified by local distortion of EG induced by the STM or AFM tip.

2. Experimental section

EG on a Si-terminated 6H-SiC(0001) surface was produced by thermal desorption of Si into a UHV chamber, following the procedure described in ref. 49. After this treatment, the samples were transferred in air to the UHV chamber (base pressure 5×10^{-10} mbar) of the combined STM/AFM microscope. Then, the samples were heated at 500–600 °C during 1 h to remove the surface contamination due to atmospheric exposure, and cooled down to room temperature before STM/AFM observations.

The RT UHV combined dynamic-STM/FM-AFM system used in this study has been previously described in ref. 50. Briefly summarized, it consists of a modified variable-temperature UHV Omicron microscope working at room temperature coupled with a homemade dual preamplifier, which is connected to a NANONIS-SPECS controller.⁵¹ The self-sensing probe consists of a qPlus sensor equipped with a tip made from platinum/iridium (Pt/Ir) or carbon fiber (CF). The fabrication process and characterization of the tips are detailed in ref. 52 for Pt/Ir tips, and in ref. 53 for CF tips. These tips were characterized by field electron emission and their curvature radii were estimated from Fowler–Nordheim plots.⁵⁴ Only tips with an apex radius below 10 nm are glued on the free prong of a qPlus probe, and qPlus sensors with a quality factor ‘Q’ above 1000 were used. Typically, the oscillation amplitude of the Pt/Ir tip was set between 0.10 and 0.15 nm and the resonance frequency was around 30 kHz.

The combined STM/AFM microscope can be operated in static and dynamic modes, depending of the feedback signal used for the tip–sample distance regulation (Fig. 1). (1) In FM-AFM operation, the feedback loop adjusts the mean Z distance between the oscillating tip and the sample in order to keep the resonance-frequency shift Δf of the qPlus sensor constant. During this operation mode, an Automatic Gain Control (AGC) adjusts the excitation signal E_{exc} of the qPlus

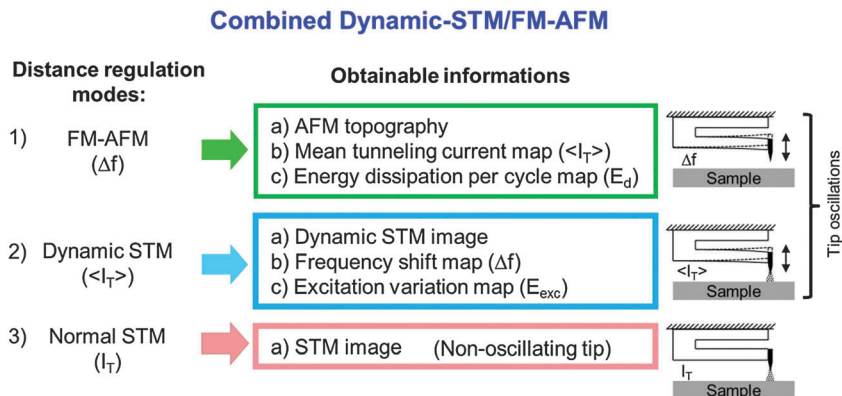


Fig. 1 Operation modes of a combined dynamic-STM/FM-AFM microscope based on a qPlus sensor: (1) FM-AFM, (2) dynamic-STM and (3) normal STM.

sensor for maintaining constant the tip oscillation amplitude above the surface. The energy dissipation per cycle E_d caused by the tip-sample interaction can be estimated from the additional increase of the excitation signal E_{exc} ^{55,56} using eqn (1):

$$E_d = \pi k A_0^2 / Q [E_{exc} / E_{exc0} - f / f_0], \quad (1)$$

where k is the spring constant of the qPlus sensor, E_{exc0} and f_0 represent the excitation signal and the free resonance frequency without any tip-surface interaction, E_{exc} and f represent the excitation signal and the resonance frequency during the tip-surface interaction while Q and A_0 represent the quality factor and the oscillating amplitude, of the non-interacting tip, respectively. In addition, a bias voltage is applied between the tip and the sample. Then, AFM topography is recorded simultaneously with maps of mean tunneling current (I_T) and excitation variations E_{exc} . (2) In dynamic-STM operation, a feedback loop regulates the mean Z distance between the oscillating tip and the sample to keep constant a time-averaged tunneling current (I_T). During operation, the tip oscillation amplitude is maintained constant. Then, dynamic STM images are simultaneously recorded with frequency shift Δf and excitation variation E_{exc} maps. It should be noted that, for small oscillation amplitudes, the variations in the frequency shift are proportional to changes in force gradients k_{ts} between the tip and sample ($k_{ts} = 2k \left(\frac{\Delta f}{f_0}\right)^{57}$), and in this operation mode, the excitation variations E_{exc} are not simply related to E_d because the tip does not oscillate at the resonance frequency of the qPlus sensor coupled with the surface. However, as the frequency shift induced by the STM tip-surface interaction remains very small (<10 Hz on ~ 30 kHz), the E_{exc} variations give qualitative information on the dissipation energy. (3) It is evident that with a non-oscillating tip, the Z distance between the tip and the sample can be adjusted to keep the tunneling current I_T constant (normal STM operation). All the data were processed using Gwyddion⁵⁸ software.

3. Results

In AFM operating in the constant frequency shift mode, the topography is simultaneously recorded together with maps of

mean tunneling current (I_T) and energy dissipation per cycle E_d variations. The images shown in Fig. 2 present periodic arrangements of clear spots corresponding to the maxima of relief (a), mean tunneling current (b), and energy dissipation per cycle (c) for the AFM regulating conditions. The spots are organized in a hexagonal lattice with a 1.9 nm period that corresponds to the (6×6) quasi-cell (green diamond) previously reported for epitaxial graphene on a reconstructed 6H-SiC(0001) surface by STM or AFM.³⁸ Interestingly, we notice that the maxima of energy dissipation per cycle and those of tunneling current in the corresponding maps do not overlap the bump relief as underlined by the white hexagons located in the same place on these images. In order to examine the relative position of these maxima, cross-section profiles along the same [11] direction of the (6×6) lattice are displayed in Fig. 3. As shown by the vertical lines, the bumps in the topography correspond to minima in the mean tunneling current and energy dissipation maps while the maxima of energy dissipation are located in the middle of the distance separating the relief bumps. Now considering the mean tunneling current variations along the [11] direction of the (6×6) quasi-cell, two remarkable features have been observed: the mean tunneling current varies asymmetrically between the relief bumps and the tunneling current maxima are typically located at 1/3 of the relief bump period along the [11] direction. The same features were observed for different experimental conditions: (i) when the tip scans the surface in the opposite direction (backward scan), as shown in the ESI† (Fig. S1), and (ii) when the tip scans the surface in FM-AFM mode to a lower frequency shift setpoint value ($\Delta f = +4$ Hz), as shown in the ESI† (Fig. S4), in which the simultaneously recorded map of mean tunneling current (I_T) shows lower (I_T) values than in Fig. 3. As such a shift between maxima in relief and tunneling current could be sensitive to the tip apex geometry, the shifts along another [11] direction of the (6×6) quasi-cell were measured in the same set of images shown in the ESI† (Fig. S2). As observed in Fig. S2 (ESI†), the non-overlapping of the topographic bumps with both the maxima of mean tunneling current and energy dissipation, which is also evidenced from the associated cross-section profiles (Fig. S3, ESI†), does not depend on the tip apex.

At a smaller scanning range, Fig. 4 presents a constant frequency shift AFM topography with a simultaneously recorded

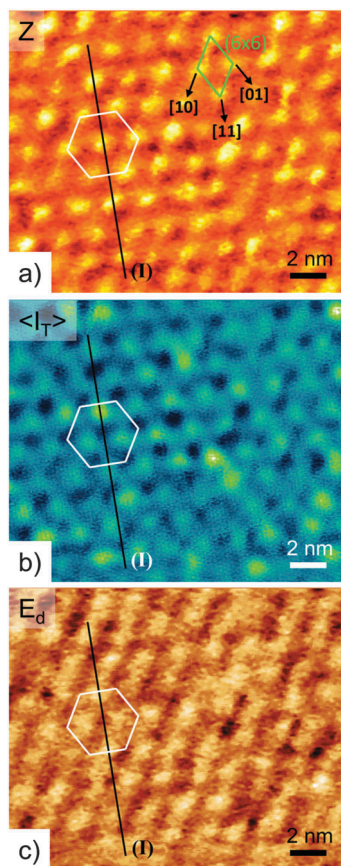


Fig. 2 (a) FM-AFM topography of epitaxial graphene on 6H-SiC(0001) obtained with a constant frequency shift (Δf) equal to +20 Hz together with simultaneously recorded maps of mean tunneling current ' $\langle I_T \rangle$ ' (b) and energy dissipation per cycle ' E_d ' variation (c). FM-AFM regulation: oscillation amplitude = 0.13 nm, $V_T = -5$ mV (forward scan direction). Z range: 0–154 pm, $\langle I_T \rangle$: 18.2–36.7 nA, E_d range: 2.08–2.65 eV per cycle. A plane fit (i), a background subtraction by matching height median (ii), a 2D FFT filter (iii) and a Gaussian smoothing correction (iv) have been performed on these images as follows: (i–iv) in (a), (ii and iii) in (b), and (ii–iv) in (c).

mean tunneling current map. Bumps in AFM topography overlap with minima in the mean tunneling current map as highlighted by the white hexagons located in the same place on these images and illustrated in the cross-section profiles (Fig. 5). In accordance with Fig. 2, the maxima of the mean tunneling current during the AFM scanning appear shifted by ~ 1 nm with respect to the topographic bumps. Besides this 1.9 nm period in the mean tunneling current map, which corresponds well to the (6×6) quasi-cell (green diamond) in the AFM topography, there is a modulation with a 0.24 nm period as shown in the mean tunneling current profile (Fig. 5(b)). This short period is assigned to the graphene honeycomb lattice, which is not detected in the AFM topography. The same features were observed when the tip scans the surface in the opposite direction (backward scan), as shown in the ESI† (Fig. S5).

Secondly, we have analyzed the images recorded in the dynamic-STM mode. A typical dynamic-STM image and the corresponding maps of variations of frequency shift and excitation signal are reported in Fig. 6. The dynamic STM image (Fig. 6(a))

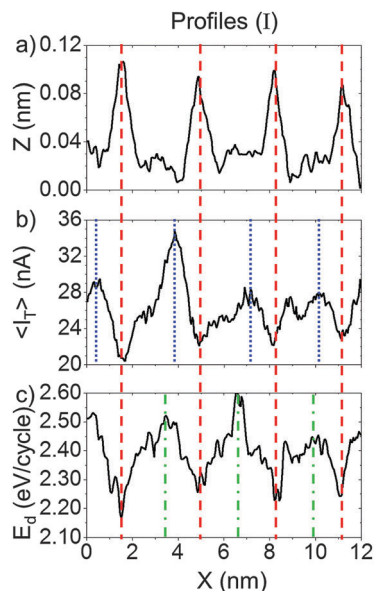


Fig. 3 Topography, mean tunneling current and energy dissipation per cycle profiles extracted from the images of Fig. 2. The cross-section profiles (I) along the [11] direction of the (6×6) quasi-cell are reported for each image in (a), (b), and (c).

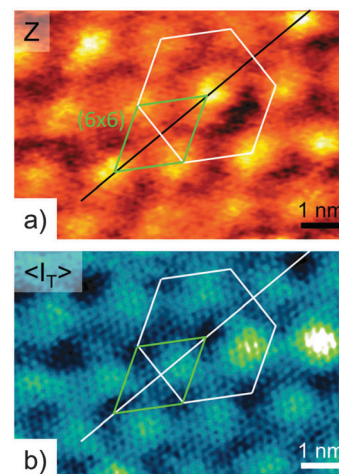


Fig. 4 (a) FM-AFM topography of epitaxial graphene on 6H-SiC(0001) obtained with a constant frequency shift (Δf) equal to +20 Hz together with a simultaneously recorded map of mean tunneling current ' $\langle I_T \rangle$ ' (b). FM-AFM regulation: oscillation amplitude = 0.13 nm, $V_T = -5$ mV (forward scan direction). Z range: 0–113 pm, $\langle I_T \rangle$ range: 20.6–36.4 nA. A plane fit (i), a background subtraction by matching height median (ii), a 2D FFT filter (iii) and a Gaussian smoothing correction (iv) have been performed on these images as follows: (i–iv) in (a) and (ii, iii) in (b).

shows a hexagonal periodic arrangement of white spots with a 1.9 nm period (red diamond). As illustrated by the white hexagons located in the same place on each image, there are contrast changes. The analysis of the three images shows that the bumps in the dynamic STM image (Fig. 6(a)) do not superimpose on maxima in the frequency shift map (Fig. 6(b)). In fact, maxima in the dynamic-STM image correspond to minima in the frequency shift as displayed in the cross-section profiles (Fig. 7(a) and (b)).

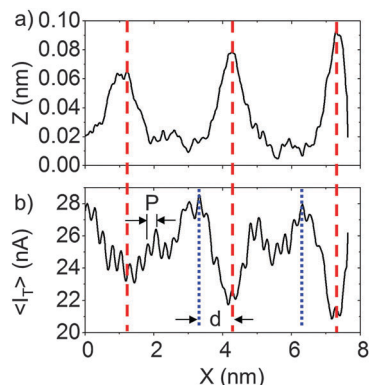


Fig. 5 Topography and mean tunneling current profiles extracted from the images of Fig. 4. The cross-section profiles along the [11] direction of the (6×6) quasi-cell are reported for each image in (a) and (b) ($P = 0.24$ nm, $d \sim 1$ nm).

Considering the STM regulation, this means that the tip–surface interaction force gradient is lower above the maxima of LDOS. In contrast, the maxima of the excitation signal are not located in the middle of the distance separating the relief bumps in the dynamic-STM image as laid out in the cross-section profiles (Fig. 7(a) and (c)). The maxima of the excitation signal are typically located at 1/3

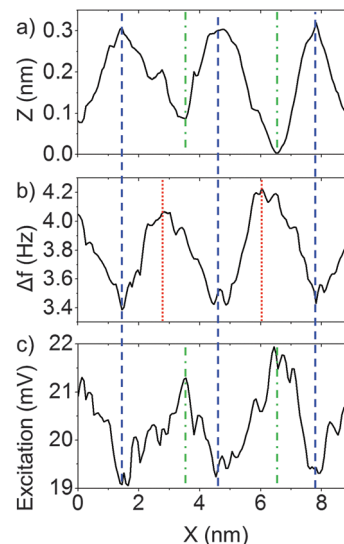


Fig. 7 Dynamic-STM, frequency shift and excitation signal profiles extracted from the images of Fig. 6. The cross-section profiles along the [11] direction of the (6×6) quasi-cell are reported for each image in (a–c).

(2/3) of the distance between the relief bumps in the dynamic-STM image in contrast to the findings obtained in AFM measurements as shown in Fig. 3.

For bias tension $|V_T| < 1$ V, the maxima in FM-AFM topographic images (dynamic STM images) are always found displaced (spatially) in comparison with the maxima of the mean tunneling current (frequency shift) map for different setpoint values of positive frequency shift (mean tunneling current).

4. Discussion

All the data obtained in this study show that maxima in dynamic-STM or FM-AFM images do not overlap with maxima in the associated maps of frequency shift or mean tunneling current maps, respectively. As the measured shift between these maxima is typically 1 nm along the [11] direction of the (6×6) quasi-cell, a question arises: is the real topography of EG on 6H-SiC(0001) reproduced by STM images?

As the role of the tip apex is crucial for surface analysis using a combined STM/AFM microscope, we first consider the influence of the tip geometry on the images. Fig. 2 and 3 together with Fig. S1–S3 (ESI[†]) demonstrate that the non-overlapping of maxima in STM (AFM) images with maxima in the frequency shift map (mean tunneling current map) is independent of the tip apex shape or the scanning direction.

Then the influence of the conductance conditions is checked. During FM-AFM imaging of graphene on 6H-SiC(0001) simultaneously recorded together with maps of mean tunneling current (Fig. 2 and 4), we obtain an average conductance value of $G = 0.25G_0$ (ESI[†]) lower than the “contact” conductance values reported by Altenburg *et al.*⁵⁹ ($0.4G_0 < G < 1.0G_0$, for graphene on Ru(0001)) and close to those obtained by other authors in STM images of graphene on Ir(111) ($G = 0.13G_0$, conditions: $I_T = 1$ μ A, $V_T = +100$ mV)⁶⁰ and graphene on Ni(111) ($G = 0.31G_0$,

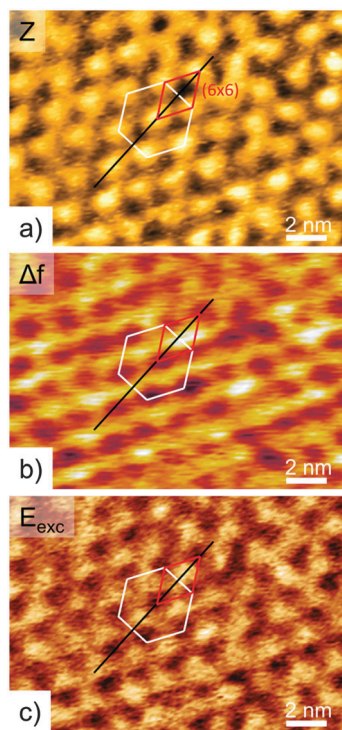


Fig. 6 (a) Dynamic-STM image of epitaxial graphene on the reconstructed 6H-SiC(0001) surface obtained using an oscillating tip. (b and c) Associated maps of the frequency shift and excitation signal simultaneously recorded with the dynamic-STM image (a). Dynamic-STM regulation: $V_T = -0.5$ V, $\langle I_T \rangle = 10$ pA. Z range is 382 pm, Δf range is 2.92–4.37 Hz, excitation signal range is 18.5–22.4 mV. A plane fit (i), a background subtraction by matching height median (ii), and a 2D FFT filter (iii) have been performed on these images as follows: (i–iii) in (a) and (iii) in (b).

conditions: $I_T = 48$ nA, $V_T = +2$ mV).⁶¹ We also remark that, during FM-AFM imaging to a lower frequency shift setpoint value of +4 Hz, the average conductance value is reduced to $G \sim 0.01G_0$ (Fig. S4, ESI†). Furthermore, the mechanical stability of the tip oscillation was assured when the AFM topography was imaged with different Δf setpoint values (for $\Delta f = +4$ (Fig. S4, ESI†) to +15 Hz (results not shown here)) and no abrupt changes (or reduction to zero) in the oscillation amplitude were observed (the tip oscillation amplitude is maintained constant, as mentioned in the Experimental section). We also pointed out that for the dynamic STM image shown in Fig. 6, the calculated conductance is much less $G = 0.97 \times 10^{-6}G_0$ (for $\langle I_T \rangle = 10$ pA, $V_T = -0.5$ V) than the conductance values in AFM images, and is in accordance with the ones obtained by other authors in STM images of graphene on SiC(0001) ($G = 1.61 \times 10^{-6}G_0$ (for $I_T = 100$ pA, $V_T = -0.8$ V)⁶² and $G = 6.45 \times 10^{-6}G_0$ (for $I_T = 100$ pA, $V_T = -0.2$ V)¹⁹). Therefore, the lateral shift between maxima in STM or AFM images with maxima in the frequency shift map or the mean tunneling current map, respectively, does not depend on the tunneling conductance for $10^{-5}G_0 < G < 0.25G_0$.

In our AFM experiments, we worked in the repulsive regime with positive frequency shift values (between +4 and +20 Hz), which were required for measuring a tunneling current. We have not detected a tunneling current in the attractive regime.

The interpretation of constant mean tunneling current STM images and those obtained with an AFM in frequency modulation mode working in repulsive interaction are usually related to constant local density of states near the Fermi level and constant total density of states (Pauli repulsion), respectively. In this simple framework, the experimental images obtained in this study suggest the existence of a shift between the maxima of total DOS corresponding to real relief and the maxima of LDOS in the EG on the reconstructed 6H-SiC(0001) surface. Nonetheless, two independent DFT calculations of the EG on 6H-SiC(0001) have shown that the maxima of LDOS are related to the carbon atoms in the underlying buffer layer, which are not chemically bonded to Si atoms of the 6H-SiC(0001) surface.^{19,34} As a result, the maxima of LDOS and then the protrusions in simulated STM images were found to be associated with the topographic bumps in calculated AFM images.

As a typical 1 nm shift is observed between the maxima in STM (AFM) images and those in the associated maps, a detailed analysis is then required for an in-depth understanding of the data recorded using the combined dynamic-STM/FM-AFM microscope.

Our qualitative analysis is based on two main arguments: Firstly, we highlight the difference between the LDOS and the total DOS profiles in the buffer layer on 6H-SiC(0001) as shown by DFT calculations. Secondly, we consider the variable decrease of the distance between the EG and the buffer layer in relation to the mechanical distortion of graphene on 6H-SiC(0001) induced by the tip.³⁸ Both causes lead to an apparent increase of the LDOS of the distorted EG monolayer and then of the measured 'relief' in the STM images.

Let us consider the maps of the total DOS and LDOS of the buffer layer obtained from DFT calculations. The total DOS

map presents a (6×6) quasi-cell of the localized maxima as shown in Fig. 1(a) of ref. 19. In contrast, the simulated STM image obtained by Kim *et al.*³⁴ from calculated LDOS of the buffer layer shows an asymmetric shaped LDOS maxima. The stretched maxima along the [11] direction find their origin in the lattice misfit between the carbon arrangement in the buffer layer and the 6H-SiC(0001) surface lattice. Despite these small differences between the LDOS and the total DOS of the buffer layer (also observed in the case of EG on SiC), the simulated STM image and AFM topography of EG on SiC, obtained from these calculations, exhibit maxima in the same place.^{19,34} Therefore, the origin of the 1 nm shift observed between AFM images and mean tunneling current maps or dynamic-STM images and frequency shift maps obtained in this study needs further research.

We believe that the observed shifts in this study originate from the tip-induced mechanical distortion³⁸ that locally modifies the electronic coupling between the EG and the buffer layer along the [11] direction of the (6×6) quasi-cell. In the schematic diagram shown in Fig. 8, the profiles of the total DOS and LDOS of the buffer layer along a [11] direction are presented together with the traces of the AFM tip and the variation of the corresponding mean tunneling current ($\langle I_T \rangle$) and energy dissipation (E_d) maps. The LDOS profile of the buffer layer was deduced from Fig. 2 of ref. 34. As a result of the distortion of the EG due to the AFM tip, the distance between the EG and the buffer layer is reduced, resulting in an increased electronic coupling. As a consequence, the LDOS of the distorted graphene increases and the mean tunneling current, which is proportional to the LDOS of distorted graphene, measured by the AFM tip, increases. In this framework, the variation of the tunneling current has been qualitatively estimated from the gap between the distorted graphene and the LDOS of the buffer layer: the tunneling current increases when the tip approaches the LDOS of the buffer layer. In addition, the position of the maxima in the $\langle I_T \rangle$ map appears to shift along the [11] direction as compared to the topographical bumps shown in Fig. 8, in agreement with experimental results (Fig. 2–5).

Let us now consider the case of the maxima in the dynamic STM images, which are spaced with respect to the position of maxima in the frequency shift map. A qualitative analysis appears awkward, because the STM tip traces a constant LDOS profile of a distorted graphene. However, considering the positive value of the measured frequency shift (repulsive regime) during STM imaging, we have demonstrated that the graphene is distorted by the STM tip. Then the ~ 1 nm shift observed between the maxima in dynamic-STM image with that of the frequency shift map originates in the tip induced distortion of EG consistently with the AFM observations. This is also supported by the location of the maxima of the excitation signal, which are situated at 1/3 (2/3) of the distance between the maxima in the dynamic-STM image in Fig. 6 (along the [11] direction of the (6×6) quasi-cell) and not in the middle as in the AFM measurements.³⁸

Clearly, this study at the nanometer scale demonstrates that the tip-induced distortion strongly influences the STM images

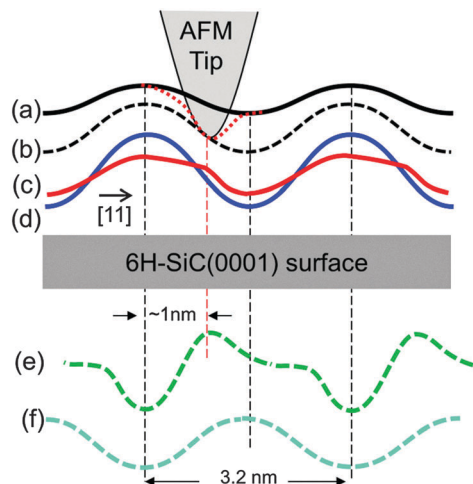


Fig. 8 Schematic view of the AFM tip-induced distortion of the epitaxial graphene on the reconstructed 6H-SiC(0001) surface along the [11] direction of the (6×6) quasi-cell. (a) Non-distorted epitaxial graphene layer (solid black line), (d) buffer layer (total DOS, solid blue line), (b) trajectory of the AFM tip end in repulsive mode (black dashed line), graphene locally distorted by the AFM tip (red dotted line), (c) LDOS of the buffer layer extracted from Fig. 2 in ref. 34 (red solid line), (e) mean tunneling current between the distorted graphene monolayer and the tip during AFM scan, and (f) variation in the energy dissipation during AFM scan (cyan dashed line).

of EG on the 6H-SiC(0001) surface. Additionally, a variation of the tip–surface force gradient during dynamic STM investigations is also evidenced at the atomic level as shown in Fig. S6 (ESI[†]). During the acquisition of a constant mean tunneling current STM image, a variation of the tip–surface force gradient ranging from 0.3 to 0.9 N m⁻¹ with a 0.24 nm lattice period was measured. Such a variation implies some tip-induced distortions of the graphene topography yielding a STM image of the graphene at the atomic level, which is different from a constant LDOS map of the non-distorted graphene.

In this work, we have demonstrated that the mechanical distortion induced by the STM tip influences the “relief” in the STM images of EG on 6H-SiC(0001) at both nanometric and atomic scales. Notably, we have found that STM images do not reproduce the real topography of EG on 6H-SiC(0001), as the positions of topographic bumps of EG on 6H-SiC(0001) are spaced typically by 1 nm from the maxima in STM images along the [11] direction of the (6×6) quasi-cell. In order to illustrate their real arrangement, we have added white triangles onto a STM image indicating the position of the topographic bumps (Fig. 9). This model is supported by the location of the maxima of the excitation signal during recording of the STM image and those of the dissipation energy during the AFM measurements.³⁸

Consequently, an extended analysis of EG on a reconstructed 6H-SiC(0001) surface based on a comparison between experimental STM images and images derived from DFT calculations requires taking the graphene distortion generated by the tip into account. However, such a quantitative analysis would necessitate information on the tip shape at the atomic level and also on the elastic properties of EG on reconstructed 6H-SiC(0001) in order

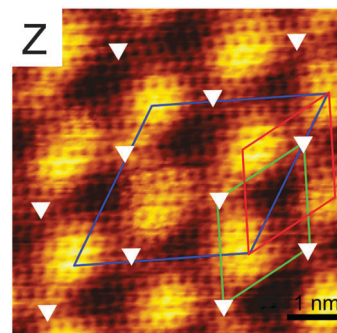


Fig. 9 A typical experimental STM image of EG on the 6H-SiC(0001) showing the $(6\sqrt{3} \times 6\sqrt{3})R30^\circ$ reconstruction (blue diamond). The real positions of the topographical bumps determined from frequency shift map are shown by white triangles. The same (6×6) quasi-cell can be recognized in the topography (green diamond) and in the tip-induced STM image (red diamond) because the maxima in the STM image are spaced by ~ 1 nm along the [11] direction of the (6×6) quasi-cell. A plane fit and a background subtraction by matching height median have been performed on the STM image. $V_T = -50$ mV, $I_T = 300$ pA and Z scale = 64 pm.

to reproduce the distortions of EG induced by the tip during STM and/or AFM studies.

5. Conclusion

A combined dynamic-STM/FM-AFM platform was used for studying epitaxial graphene on the reconstructed 6H-SiC(0001) surface at room temperature under UHV conditions.

STM and AFM images independently recorded present the same lattice of bumps with a 1.9 nm period that is attributed to the (6×6) quasi-cell, in agreement with the DFT calculations and previously reported experimental results. However, topographic bumps (AFM) and maxima in the simultaneously recorded map of mean tunneling current appeared spaced by typically 1 nm along the [11] direction of the (6×6) quasi-cell. The same shift is observed when the location of maxima in STM images is compared to the maxima in the associated map of frequency shift. In both experiments, the tip–sample interaction is repulsive, and the results were verified for tunneling conductance values ranging from $10^{-5}G_0$ to $0.25G_0$. Consequently, the real topography of EG on reconstructed 6H-SiC(0001) given by constant frequency shift AFM images does not correspond to the corrugations shown by STM images.

From a detailed image comparison, the origin of these shifts is attributed to variations of coupling between the local density of states (LDOS) of EG and the LDOS of the buffer layer amplified by local distortion of epitaxial graphene induced by the tip due to repulsive interaction with the sample. As a consequence, the measured corrugation in constant mean tunneling current STM images mixes the LDOS variation of EG with the tip-induced mechanical distortion of graphene, whose amplitude varies along the [11] direction of the (6×6) quasi-cell. The location of the maxima of the excitation signal during recording of STM images and those of the dissipation energy during the AFM measurements supports this model.

Furthermore, graphene distortions have been detected at the atomic level resulting from modulations of the tip/surface force gradient with a 0.24 nm period induced by the STM tip.

Finally this combined STM-AFM study of EG on a reconstructed 6H-SiC(0001) surface demonstrates that a constant current STM image does not reproduce its real topography but corresponds to the measured LDOS modulations, which depend on the variable tip-induced graphene distortion within the (6 × 6) quasi-cell at the atomic scale. Therefore to achieve an in-depth understanding of STM or AFM images and/or to compare their relief with DFT calculations, the mechanical distortion of epitaxial graphene induced by the tip must be taken into account in new studies.

Acknowledgements

The authors wish to thank A. Ouerghi ((CNRS-LPN), Route de Nozay, 91460 Marcoussis, France) who kindly provided the epitaxial graphene samples as well as J. Polesel-Maris (LIST/MRT, 41 rue du Brill, L-4422 Belvaux, Luxembourg) for the dedicated efforts in the development of the RT-UHV combined STM/AFM microscope.

José Antonio Morán Meza would also like to acknowledge financial support from Réseau Thématique de Recherche Avancée (RTRA-Triangle de la Physique) and CEA/Direction des Relations Internationales (DRI).

References

- 1 A. K. Geim and K. S. Novoselov, *Nat. Mater.*, 2007, **6**, 183–191.
- 2 K. S. Novoselov, A. K. Geim, S. V. Morozov, D. Jiang, Y. Zhang, S. V. Dubonos, I. V. Grigorieva and A. A. Firsov, *Science*, 2004, **306**, 666–669.
- 3 J. Wintterlin and M.-L. Bocquet, *Surf. Sci.*, 2009, **603**, 1841–1852.
- 4 C. Berger, Z. Song, T. Li, X. Li, A. Y. Ogbazghi, R. Feng, Z. Dai, A. N. Marchenkov, E. H. Conrad, P. N. First and W. A. de Heer, *J. Phys. Chem. B*, 2004, **108**, 19912–19916.
- 5 C. Virojanadara, R. Yakimova, A. A. Zakharov and L. I. Johansson, *J. Phys. D: Appl. Phys.*, 2010, **43**, 374010.
- 6 K. V. Emtsev, A. Bostwick, K. Horn, J. Jobst, G. L. Kellogg, L. Ley, J. L. McChesney, T. Ohta, S. A. Reshanov, J. Röhr, E. Rotenberg, A. K. Schmid, D. Waldmann, H. B. Weber and T. Seyller, *Nat. Mater.*, 2009, **8**, 203–207.
- 7 H.-S. Tsai, C.-C. Lai, H. Medina, S.-M. Lin, Y.-C. Shih, Y.-Z. Chen, J.-H. Liang and Y.-L. Chueh, *Nanoscale*, 2014, **6**, 13861–13869.
- 8 Y. Lin, C. Dimitrakopoulos, K. A. Jenkins, D. B. Farmer, H. Chiu, A. Grill and P. Avouris, *Science*, 2010, **327**, 662.
- 9 J. Baringhaus, M. Ruan, F. Edler, A. Tejada, M. Sicot, A. Taleb-Ibrahimi, A.-P. Li, Z. Jiang, E. H. Conrad, C. Berger, C. Tegenkamp and W. A. de Heer, *Nature*, 2014, **506**, 349–354.
- 10 W. Chen, H. Xu, L. Liu, X. Gao, D. Qi, G. Peng, S. C. Tan, Y. Feng, K. P. Loh and A. T. S. Wee, *Surf. Sci.*, 2005, **596**, 176–186.
- 11 C. Riedl and U. Starke, *Phys. Rev. B*, 2007, **76**, 245406.
- 12 C. Virojanadara, M. Syväjarvi, R. Yakimova, L. Johansson, A. Zakharov and T. Balasubramanian, *Phys. Rev. B*, 2008, **78**, 245403.
- 13 K. V. Emtsev, F. Speck, T. Seyller and L. Ley, *Phys. Rev. B*, 2008, **77**, 155303.
- 14 U. Starke and C. Riedl, *J. Phys.: Condens. Matter*, 2009, **21**, 134016.
- 15 C. Riedl, C. Coletti and U. Starke, *J. Phys. D: Appl. Phys.*, 2010, **43**, 374009.
- 16 V. W. Brar, Y. Zhang, Y. Yayon, T. Ohta, J. L. McChesney, A. Bostwick, E. Rotenberg, K. Horn and M. F. Crommie, *Appl. Phys. Lett.*, 2007, **91**, 122102.
- 17 G. M. Rutter, N. P. Guisinger, J. N. Crain, E. A. A. Jarvis, M. D. Stiles, T. Li, P. N. First and J. A. Stroscio, *Phys. Rev. B: Condens. Matter Mater. Phys.*, 2007, **76**, 235416.
- 18 P. Mallet, F. Varchon, C. Naud, L. Magaud, C. Berger and J.-Y. Veuille, *Phys. Rev. B: Condens. Matter Mater. Phys.*, 2007, **76**, 041403.
- 19 F. Varchon, P. Mallet, J.-Y. Veuille and L. Magaud, *Phys. Rev. B: Condens. Matter Mater. Phys.*, 2008, **77**, 235412.
- 20 P. Lauffer, K. V. Emtsev, R. Graupner, T. Seyller and L. Ley, *Phys. Rev. B: Condens. Matter Mater. Phys.*, 2008, **77**, 155426.
- 21 Y. Qi, S. H. Rhim, G. F. Sun, M. Weinert and L. Li, *Phys. Rev. Lett.*, 2010, **105**, 085502.
- 22 S. Forti, K. V. Emtsev, C. Coletti, A. A. Zakharov, C. Riedl and U. Starke, *Phys. Rev. B: Condens. Matter Mater. Phys.*, 2011, **84**, 125449.
- 23 J. Choi, H. Lee and S. Kim, *J. Phys. Chem. C*, 2010, **114**, 13344–13348.
- 24 S. Goler, C. Coletti, V. Piazza, P. Pingue, F. Colangelo, V. Pellegrini, K. V. Emtsev, S. Forti, U. Starke, F. Beltram and S. Heun, *Carbon*, 2013, **51**, 249–254.
- 25 T. Filleter, K. V. Emtsev, T. Seyller and R. Bennewitz, *Appl. Phys. Lett.*, 2008, **93**, 133117.
- 26 T. Filleter and R. Bennewitz, *Phys. Rev. B: Condens. Matter Mater. Phys.*, 2010, **81**, 155412.
- 27 C. Held, T. Seyller and R. Bennewitz, *Beilstein J. Nanotechnol.*, 2012, **3**, 179–185.
- 28 M. Telychko, J. Berger, Z. Majzik, P. Jelínek and M. Švec, *Beilstein J. Nanotechnol.*, 2015, **6**, 901–906.
- 29 F. Castanić, L. Nony, S. Gauthier and X. Bouju, *Beilstein J. Nanotechnol.*, 2012, **3**, 301–311.
- 30 D. S. Wastl, A. J. Weymouth and F. J. Giessibl, *ACS Nano*, 2014, **8**(5), 5233–5239.
- 31 V. W. Brar, Y. Zhang, Y. Yayon, T. Ohta, J. L. McChesney, A. Bostwick, E. Rotenberg, K. Horn and M. F. Crommie, *Appl. Phys. Lett.*, 2007, **91**, 122102.
- 32 A. Mattausch and O. Pankratov, *Phys. Rev. Lett.*, 2007, **99**, 076802.
- 33 F. Varchon, R. Feng, J. Hass, X. Li, B. Nguyen, C. Naud, P. Mallet, J.-Y. Veuille, C. Berger, E. Conrad and L. Magaud, *Phys. Rev. Lett.*, 2007, **99**, 126805.
- 34 S. Kim, J. Ihm, H. Choi and Y.-W. Son, *Phys. Rev. Lett.*, 2008, **100**, 176802.
- 35 J. Hass, W. A. de Heer and E. H. Conrad, *J. Phys.: Condens. Matter*, 2008, **323202**, 1–27.

- 36 M. Hupalo, E. H. Conrad and M. C. Tringides, *Phys. Rev. B: Condens. Matter Mater. Phys.*, 2009, **80**, 1–4.
- 37 J.-Y. Veuillen, F. Hiebel, L. Magaud, P. Mallet and F. Varchon, *J. Phys. D: Appl. Phys.*, 2010, **43**, 374008.
- 38 J. A. Morán Meza, C. Lubin, F. Thoyer and J. Cousty, *Nanotechnology*, 2015, **26**, 255704.
- 39 G. F. Sun, J. F. Jia, Q. K. Xue and L. Li, *Nanotechnology*, 2009, **20**, 355701.
- 40 E. Stolyarova, D. Stolyarov, L. Liu, K. T. Rim, Y. Zhang, M. Han, M. Hybersten, P. Kim and G. Flynn, *J. Phys. Chem. C*, 2008, **112**, 6681–6688.
- 41 N. N. Klimov, S. Jung, S. Zhu, T. Li, C. A. Wright, S. D. Solares, D. B. Newell, N. B. Zhitenev and J. A. Stroscio, *Science*, 2012, **336**, 1557–1561.
- 42 S. Koch, D. Stradi, E. Gnecco, S. Barja, S. Kawai, C. Diaz, M. Alcamí, F. Martin, A. Vasquez, R. Miranda, T. Glatzel and E. Meyer, *ACS Nano*, 2013, **7**(4), 2927–2934.
- 43 F. J. Giessibl, S. Hembacher, J. Mannhart and C. F. Quate, *Proc. Natl. Acad. Sci. U. S. A.*, 2003, **100**, 12539–12542.
- 44 S. Kawai and H. Kawakatsu, *Phys. Rev. B: Condens. Matter Mater. Phys.*, 2009, **79**, 115440.
- 45 E. N. Voloshina, Y. S. Dedkov, S. Torbrügge, A. Thissen and M. Fonin, *Appl. Phys. Lett.*, 2012, **100**, 241606.
- 46 Y. S. Dedkov, E. N. Voloshina, E. Fertitta, A. Garhofer, F. Mittendorfer, M. Fonin and A. Thissen, *Sci. Rep.*, 2013, **3**, 1072.
- 47 S. J. Altenburg and R. Berndt, *New J. Phys.*, 2014, **16**, 053036.
- 48 J. M. Soler, A. M. Baro, N. Garcia and H. Rohrer, *Phys. Rev. Lett.*, 1986, **57**(4), 444–447.
- 49 J. Penuelas, A. Ouerghi, D. Lucot, C. David and J. Gierak, *Phys. Rev. B: Condens. Matter Mater. Phys.*, 2009, **79**, 033408.
- 50 J. Polesel-Maris, C. Lubin, F. Thoyer and J. Cousty, *J. Appl. Phys.*, 2011, **109**, 074320.
- 51 *Nanonis-SPECS Zurich GmbH, Technoparkstrasse 1*, 8005 Zurich, Switzerland, 2013.
- 52 J. A. Morán Meza, J. Polesel-Maris, C. Lubin, F. Thoyer, A. Ouerghi and J. Cousty, *Curr. Appl. Phys.*, 2015, **15**, 1015–1021.
- 53 J. A. Morán Meza, C. Lubin, F. Thoyer, K. A. Villegas Rosales, A. A. Gutarra Espinoza, F. Martin and J. Cousty, *Carbon*, 2015, **86**, 363–370.
- 54 R. H. Fowler and L. Nordheim, *Proc. R. Soc. London, Ser. A*, 1928, **119**, 173–181.
- 55 B. Gotsmann, C. Seidel, B. Anczykowski and H. Fuchs, *Phys. Rev. B: Condens. Matter Mater. Phys.*, 1999, **60**(15), 51–61.
- 56 A. Farrell, T. Fukuma, T. Uchihashi, E. Kay, G. Bottari, D. Leigh, H. Yamada and S. Jarvis, *Phys. Rev. B: Condens. Matter Mater. Phys.*, 2005, **72**, 125430.
- 57 F. J. Giessibl, *Rev. Mod. Phys.*, 2003, **75**, 949–983.
- 58 D. Nečas and P. Klapetek, *Cent. Eur. J. Phys.*, 2011, **10**(1), 181–188.
- 59 S. J. Altenburg, J. Kröger, B. Wang, M. L. Bocquet, N. Lorente and R. Berndt, *Phys. Rev. Lett.*, 2010, **105**, 1–4.
- 60 S. J. Altenburg and R. Berndt, *New J. Phys.*, 2014, **16**, 053036.
- 61 Y. Dedkov, E. Voloshina and M. Fonin, *Phys. Status Solidi*, 2015, **252**, 451–468.
- 62 C. Berger, Z. Song, X. Li, X. Wu, N. Brown, C. Naud, D. Mayou, T. Li, J. Hass, A. N. Marchenkov, E. H. Conrad, P. N. First and W. a. de Heer, *Science*, 2006, **312**, 1191–1196.